

Cite this: *Chem. Sci.*, 2024, **15**, 2167

All publication charges for this article have been paid for by the Royal Society of Chemistry

Facile electrocatalytic proton reduction by a [Fe–Fe]-hydrogenase bio-inspired synthetic model bearing a terminal CN[−] ligand†

Abhijit Nayek, ^{‡,a} Subal Dey, ^{‡,a} Suman Patra,^a Atanu Rana,^a Pauline N. Serrano,^b Simon J. George, ^{bd} Stephen P. Cramer,^{bcd} Somdatta Ghosh Dey^{*a} and Abhishek Dey^{*a}

An azadithiolate bridged CN[−] bound pentacarbonyl bis-iron complex, mimicking the active site of [Fe–Fe] H₂ase is synthesized. The geometric and electronic structure of this complex is elucidated using a combination of EXAFS analysis, infrared and Mössbauer spectroscopy and DFT calculations. The electrochemical investigations show that complex **1** effectively reduces H⁺ to H₂ between pH 0–3 at diffusion-controlled rates (10^{11} M^{−1} s^{−1}) i.e. 10^8 s^{−1} at pH 3 with an overpotential of 140 mV. Electrochemical analysis and DFT calculations suggests that a CN[−] ligand increases the pK_a of the cluster enabling hydrogen production from its Fe(Ⅰ)–Fe(0) state at pHs much higher and overpotential much lower than its precursor bis-iron hexacarbonyl model which is active in its Fe(0)–Fe(0) state. The formation of a terminal Fe–H species, evidenced by spectroelectrochemistry in organic solvent, via a rate determining proton coupled electron transfer step and protonation of the adjacent azadithiolate, lowers the kinetic barrier leading to diffusion controlled rates of H₂ evolution. The stereo-electronic factors enhance its catalytic rate by 3 order of magnitude relative to a bis-iron hexacarbonyl precursor at the same pH and potential.

Received 11th October 2023
Accepted 22nd December 2023

DOI: 10.1039/d3sc05397k
rsc.li/chemical-science

Hydrogenases (H₂ases) efficiently interconvert H⁺ to H₂ with high turnover numbers (TONs) ($10^{2–5}$ mol s^{−1}).^{1,2} Based on the metal centers present at the active site of these metalloenzymes, three types of H₂ases are known in nature – [Fe–Fe] H₂ase, [Ni–Fe] H₂ase and Fe-only H₂ase.^{3,4} Among these, the [Fe–Fe] H₂ases are more selective towards H₂ generation, the [Ni–Fe] H₂ases are selective for H₂ oxidation while the Fe-only H₂ases in the presence of a hydride acceptor/donor substrate reacts with H₂ or produce H₂.^{5,6} High-resolution X-ray crystal structure of the that [Fe–Fe] H₂ase active site reveals that one of the iron centers of a Fe₂S₂(CO)₃(CN)₂ organometallic core (2Fe subsite) is attached to a [Fe₄S₄] cluster through a bridging cysteine (Scheme 1A and B).^{4,7,8} A key bismethyleneazadithiolate (ADT) moiety bridges between the two Fe centers of the Fe₂S₂(CO)₃(CN)₂ organometallic core. Each of the two iron centers are coordinated with one –CO ligand and one –CN[−] ligand.^{9,10} A –CO ligand bridges both

of the iron centers (Scheme 1A and B).^{7,11} The catalytic cycle of [Fe–Fe] H₂ases encompasses three primary oxidation states. These include H_{ox} (oxidized), characterized by a Fe(Ⅰ)–Fe(Ⅱ) [Fe₄S₄]²⁺ state;^{12,13} H_{red} (reduced), denoting a Fe(Ⅰ)–Fe(Ⅰ)[Fe₄S₄]²⁺ state; and H_{sred} (super reduced), which manifests as a Fe(Ⅰ)–Fe(Ⅰ)[Fe₄S₄]⁺ state.^{14–16} The unique catalytic capability of the H₂ cluster is attributed, among other factors, to a distinctive arrangement known as the rotated structure. This configuration introduces a vacant site at the distal iron (Fe_d) atom.^{17–21} The proposed mechanism suggests that the initial protonation occurs at the bridgehead nitrogen atom of the Fe(Ⅰ)–Fe(Ⅰ) state within the enzyme.^{14,22} A critical step in this process involves a proton relay from the bridgehead –NH group to the distal iron atom (Fe_d). This step is considered pivotal in the formation of a terminal hydride species with a amine form of the ADT bridgehead, H_{hyd}, which is characterized as a superoxidized diiron site with Fe(Ⅱ)–Fe(Ⅱ) state.^{23–27} Substrates (H⁺/H₂) along with the inhibitors like O₂ and CO, binding occurs at the distal iron centre (Fe_d).^{17,20} The synthesis and characterization of [Fe–Fe] H₂ase mimic has become a rapidly growing area of research.^{28–37} A large number of [Fe–Fe] H₂ase active site analogues have been synthesized mimicking several structural aspects of the active site and several details of electronic structure and its contribution to reaction mechanism have been elucidated.^{30,31,37–41} In particular, the role of the μ-CO ligand and

^aSchool of Chemical Science, Indian Association for the Cultivation of Science, Kolkata 700032, India. E-mail: icsgd@iacs.res.in; icad@iacs.res.in

^bDepartment of Chemistry, University of California, Davis, CA 94616, USA

^cPhysical Biosciences Division, Lawrence Berkeley National Laboratory, Berkeley, CA 94720, USA

^dSETI Institute, 339 Bernardo Ave, Suite, 200 Mountain View, CA 94043, USA

† Electronic supplementary information (ESI) available. See DOI: <https://doi.org/10.1039/d3sc05397k>

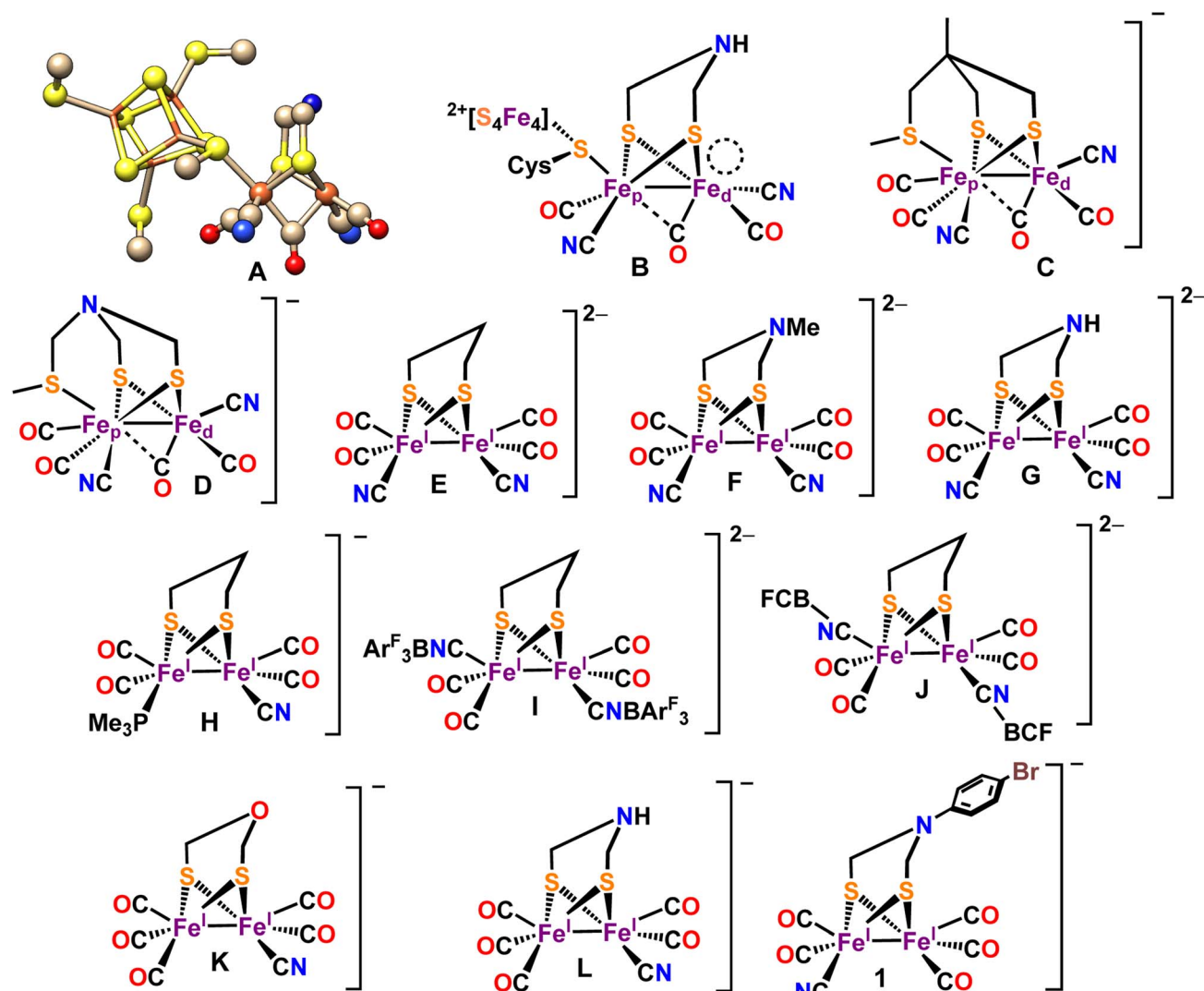
‡ These authors contributed equally to this work.



the rotated structure of the core has been a matter of great interest. After the initial report of a transient -CO bridged Fe(1)-Fe(II) complex,⁴² synthetic model complexes with $\mu\text{-CO}$ ligands have been reported.^{28,39,43} Similarly, mimics of 2Fe subsite with CN^- ligands and Lewis acid capped CN^- ligands have been reported (Scheme 1C-L).⁴⁴⁻⁵⁴

Lately, there has been several reports that it's possible to activate the $[\text{Fe-Fe}]$ H_2 ases enzyme by introducing synthetic complexes with -CN^- ligands to the apo-enzyme (which has different bridging dithiolate ligands).⁵⁵⁻⁶⁰ Recently, the formation of a miniaturized $[\text{Fe-Fe}]$ H_2 ases incorporating -CN^- ligands, has been reported. This model is generated through the combination of an oligopeptide binding $[\text{Fe}_4\text{S}_4]$ cluster and an organometallic Fe complex, and its formation has been scrutinized using various spectroscopic techniques.⁶¹ The electrocatalytic and photocatalytic behaviour for some of these synthetic analogues of $[\text{Fe-Fe}]$ H_2 ases were reported mostly in organic solvents.^{46,61,63-69} In a report by our group, a synthetic

model $p\text{-BrC}_6\text{H}_4\text{N}(\text{CH}_2\text{S})_2\text{Fe}_2\text{CO}_6$ was shown to be a very efficient catalyst for HER under aqueous condition.⁷⁰ This catalyst exhibited TON and TOF of $>>10^8$ and 6400 s^{-1} at 440 mV overpotential. Following this, several recent reports of HER by $\text{Fe}_2\text{S}_2(\text{CO})_6$ complexes have appeared in the literature.⁷¹⁻⁷³ The same $p\text{-BrC}_6\text{H}_4\text{N}(\text{CH}_2\text{S})_2\text{Fe}_2\text{CO}_6$ model has been used to investigate the mechanism of degradation of the $\text{Fe}_2\text{S}_2(\text{CO})_6$ cluster in the presence of O_2 .⁷⁴ Using these insights synthetic analogues of $[\text{Fe-Fe}]$ H_2 ases which could catalyze HER in the presence of O_2 were developed.⁷⁵ However, these complexes did not bear terminal CN^- ligands present in the active site of H_2 ase which plays a major role in the reactivity of $[\text{Fe-Fe}]$ H_2 ase.^{47,76} Synthetic models bearing terminal CN^- ligands have been reported and their ability to catalyze HER has been evaluated.^{47,52,53,77-79} However, these complexes decomposed in the presence of acid *via* protonation of the electron rich CN^- ligand and produced sub-stoichiometric H_2 .⁸⁰ Thus, the role of CN^- ligand in HER catalysis remains unexplored in synthetic models.



Scheme 1 (A) X-ray crystal structure of the "H-cluster" in the H_{ox} state in $[\text{Fe-Fe}]\text{-H}_2\text{ase}$ (PDB ID: 3C8Y⁶²). (B) Chem Draw representation of the active site of $[\text{Fe-Fe}]\text{-H}_2\text{ase}$. The vacant site at the distal iron atom is indicated by a circular ring. Reported $[\text{Fe-Fe}]$ H_2ase synthetic mimics bearing- CN ligands in H_{rest} (C-L). New synthetic mimic of $[\text{Fe-Fe}]$ H_2ase $[\text{BrC}_6\text{H}_4\text{N}(\text{CH}_2\text{S})_2\text{Fe}_2(\text{CO})_5\text{CN}^-]$ (1).



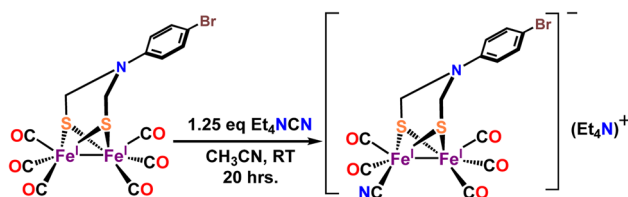
In this manuscript, we have substituted a terminal $-\text{CO}$ of a synthetic mimic $p\text{-BrC}_6\text{H}_4\text{N}(\text{CH}_2\text{S})_2\text{Fe}_2(\text{CO})_6$ by a CN^- leading to a ADT bridge synthetic mimic of the H_{red} state, $[\text{Et}_4\text{N}]^+[\text{BrC}_6\text{H}_4\text{N}(\text{CH}_2\text{S})_2\text{Fe}_2(\text{CO})_5\text{CN}]^-$ (**1**, Scheme 1). The geometric and electronic structure of complex **1** is elucidated by EXAFS, FTIR, ESI-MS, Mössbauer, ^1H -NMR and DFT calculations. The heterogeneous electrochemical hydrogen production with the complex **1** has been investigated in dil. H_2SO_4 ($\text{pH} \leq 3$) solution and the results indicate hydrogen production at very low overpotential with very high turnover rates orders of magnitude greater than those obtained for the precursor complex which does not bear the terminal CN^- ligand. While the CN^- ligand, remaining intact during electrolysis both in aqueous and organic solvents, shifts the reduction potentials more cathodic, it activates the $\text{Fe}(\text{i})\text{--Fe}(\text{0})$ state for HER catalysis

which results in a much lower overpotential for HER relative to the precursor complex which requires reduction to the $\text{Fe}(\text{0})\text{--Fe}(\text{0})$ state for HER catalysis.

Results and analysis

Synthesis and characterization

Complex **1** is synthesized *via* modification of a previously reported literature method.⁵² Addition of 1.25 eq. of $\text{Et}_4\text{N}\text{CN}$ under dark to the precursor complex $p\text{-BrC}_6\text{H}_4\text{N}(\text{CH}_2\text{S})_2\text{Fe}_2(\text{CO})_6$ in dry acetonitrile led to gradual change of color from red to reddish brown (Scheme 2). FTIR spectrum was measured after 7–8 h. That showed disappearance of vibrations for the precursor complex and appearance of several new vibrations, especially 2093 cm^{-1} band (Fig. 1A, red). The band gradually increased in intensity and the final product was isolated after 24 h. The detailed experimental procedure is described in the ESI.† The composition of the product was determined using ^1H -NMR (Fig. S10†), ^{13}C -NMR (Fig. S11†), elemental analysis, negative mode Mass spectrometry (Fig. 1B) and Mössbauer spectroscopy (Fig. 2B). In particular, the mass spectrum showed a fragmentation pattern consistent with the loss of five $-\text{CO}$ ligands present in the complex (Fig. 1B). Complex **1** showed λ_{max} at 358 nm with weaker transitions at 529 nm , 428 nm and 286 nm (Fig. S1†). The transitions below 400 nm likely represent



Scheme 2 Synthetic route for complex **1**.

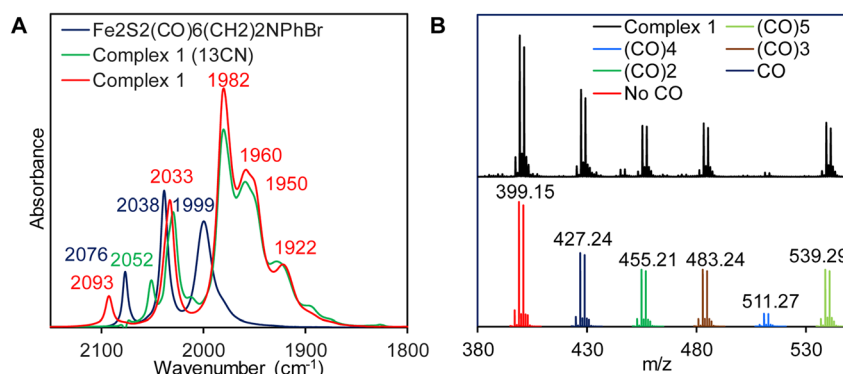


Fig. 1 (A) FTIR spectra for complex **1** (red) & its ^{13}CN analogue (green). The precursor complex is shown in blue (B) (–)ve ion mode ESI-MS of complex **1** (black) and corresponding simulated spectra with successive five CO release (bottom).

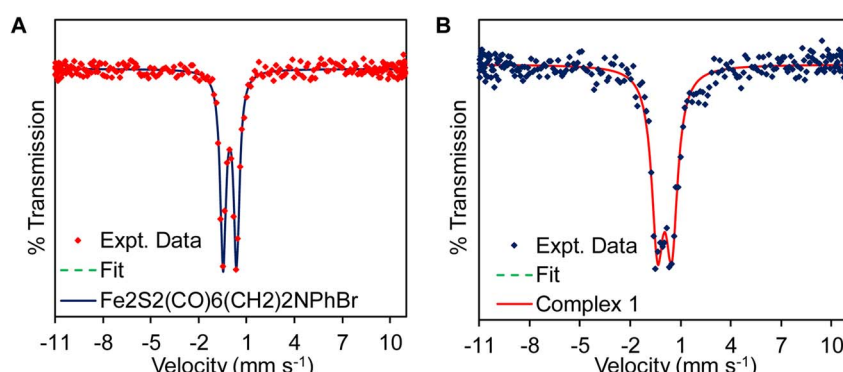


Fig. 2 Mössbauer spectra of the (A) precursor complex and (B) complex **1** recorded at 90 K .



Fe \rightarrow CO MLCT transitions. On replacing one CO in *p*-BrC₆-H₄N(CH₂S)₂Fe₂(CO)₆ complex with CN⁻ in complex **1**, these Fe \rightarrow CO MLCT transitions were shifted to lower energies. This is consistent with increase in the d manifold due to reduction of Z_{eff} because of the CN⁻ ligation.

The *p*-BrC₆H₄N(CH₂S)₂Fe₂CO₆ complex showed characteristic C–O vibrations at 2076, 2038 and 1999 cm⁻¹ (Fig. 1A, blue). These vibrations were shifted to lower energies to 2033, 1982, 1960, 1950 and 1922 cm⁻¹ in complex **1** (Fig. 1A, red). The terminal ν_{CO} vibrations of the CN⁻ bound complex **1** were red shifted relative to the neutral complex which indicates enhanced Fe–CO back bonding in the anionic complex relative to the neutral complex. The presence of a terminal CN⁻ ligand in complex **1** was inferred from the vibration at 2093 cm⁻¹ in the FTIR which shifted to lower wavenumbers upon incorporation of ¹³CN⁻ to 2052 cm⁻¹ (Fig. 1A, green). These results are well in agreement with the previously reported synthetic models of H₂ases bearing terminal CN⁻ ligand and attributes complex **1** as terminally bound mono CN⁻ substituted pentacarbonylated [2Fe]-subsite models.^{50,81,82}

The presence of -CN⁻ in complex **1** was also suggested by Mössbauer spectroscopy (Fig. 2) of the precursor complex and complex **1**. The precursor complex has an isomer shift (δ_{iso}) and quadrupole splitting (ΔE_Q) of -0.051 mm s^{-1} and 0.846 mm s^{-1} consistent with a Fe(i)-Fe(i) electronic structure description.⁸³ The δ_{iso} and ΔE_Q for complex **1** is 0.05 mm s^{-1} and 0.85 mm s^{-1} , respectively. Due to the presence of anionic -CN⁻ in complex **1**, the electron density in the diiron cluster increases and as a result the δ_{iso} of the complex **1** shift to slightly more positive values (Fig. 2B and Table 1) compared to the precursor complex, Fe₂S₂(CO)₆(CH₂)₂NPhBr (Fig. 2A and Table 1). These results are consistent with the previous reported values of -CN bound complexes.^{49,83}

In order to obtain structural parameters, several attempts to grow X-ray suitable single crystal were unsuccessful. Hence, EXAFS data of an acetonitrile solution of complex **1** are obtained at the Fe K-edge. The Fourier transform spectrum is dominated by 3 sets of peaks (Fig. 3). The strong peak at about 2.28 Å fits well to an average of 2 Fe–S interactions per Fe. At shorter distance, the peaks around 1.7–1.9 Å arise from Fe–C interactions. Detailed fitting reveals that these interactions can be separated into 2 groups, with about half occurring at an average of 1.74 Å, and the rest averaging about 1.89 Å, indicating that apart from the Fe–CN some of the Fe–CO's have longer Fe–C bond lengths. A scattering from the nitrogen of the CN⁻ ligand can be clearly picked up at 3.1 Å, indicating the presence of the CN⁻ ligand. Finally, the

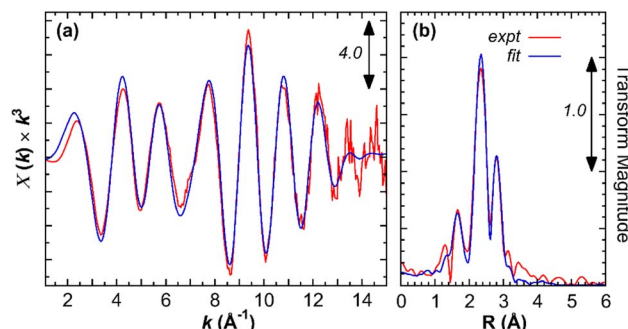


Fig. 3 Fe K-edge EXAFS spectra of complex **1**. (a) EXAFS data (red) and fit (blue). (b) Corresponding Fourier transform spectra.

Table 2 The bond distances obtained from the Fourier transformed EXAFS data

Interaction	N^a	R (Å)	σ^2 (Å ²)	ΔE^0 (eV)
Fe–S	2.0	2.280 (0.003)	0.0049 (0.0002)	-8.7(0.3)
Fe–C	1.5	1.738 (0.004)	0.0030 (0.0003)	
	1.5	1.878 (0.005)	0.0031 (0.0005)	
Fe–O (CO)	2.0	2.916 (0.003)	0.0045 (0.0002)	
Fe–N	0.5	3.106 (0.009)	0.0020 (0.0002)	
Fe–Fe	1.0	2.489 (0.002)	0.0037 (0.0006)	

^a N = Number of backscattering atoms; R = distance; σ^2 = Debye–Waller factor; ΔE^0 = threshold energy. In this fit, the backscatter atom numbers (N) are fixed to the values expected for the model while R , σ^2 , and ΔE^0 are floated. Threshold energies (ΔE^0) are constrained to be the same for all components. The estimated uncertainties in R , σ^2 , and ΔE^0 are shown in parentheses. Parameters without uncertainties in parentheses were not floated in the given fit. The scale factor used was 1.0. Phase and amplitudes were calculated using FEFF8.42.

analysis indicates the presence of a Fe–Fe interaction at 2.49 Å (Table 2).

Geometry optimized density functional theory (DFT)^{84–86} calculations are used to deduce a possible three-dimensional structure of the complex **1** pre-assuming the fact that the complex bears five -CO and a -CN⁻ ligand along with the ADT as indicated from the above spectroscopic characterizations.^{55,87,88} DFT calculations were used to validate the experimentally obtained structural and vibrational features to emulate the feasibility of -axial and -equatorial conformers (Fig. 4B and C) (where the CN⁻ ligand is either -axial or -equatorial with respect to the plane defined by the ADT moiety, *i.e.* Fe₂S₂ plane) (Fig. 4). The calculations at this level could reproduce the three-dimensional geometry and vibrational frequencies of the precursor complex reasonably (Table 3).⁷⁰ These calculations indicate that while both the conformers result in stable geometries and the optimized Fe–C, Fe–S distances are in reasonable agreement with the EXAFS data (Table 3). However, while the Fe–Fe distance in the -equatorial conformer (Fig. 4C) is 2.51 Å and agrees well with the experimental value of 2.49 Å, the Fe–Fe distance of the -axial-conformer is 2.57 Å and does not match the EXAFS data. Additionally, the -axial conformer (Fig. 4B) leads to a μ -CO ligand with ν_{CO} at 1840 cm⁻¹ (Table 3) which is not consistent

Table 1 Experimental Mössbauer parameters obtained from the experiments at 90 K

Mössbauer parameters	Fe ₂ S ₂ (CO) ₆ (CH ₂) ₂ NPhBr	Complex 1
δ_{iso} (mm s ⁻¹)	-0.051 ± 0.003	0.05 ± 0.01
ΔE_Q (mm s ⁻¹)	0.846 ± 0.001	0.85 ± 0.01



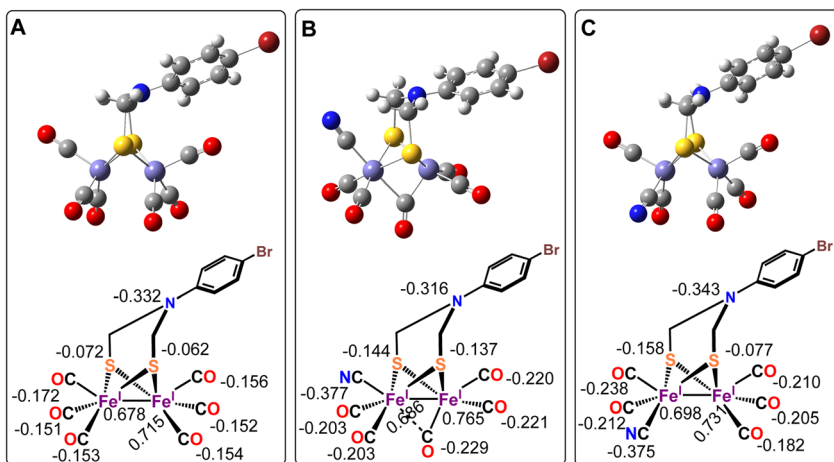


Fig. 4 Optimized geometries of *p*-BrC₆H₄N(CH₂S)₂Fe₂CO₆ complex (A, top) and complex 1 in axial-CN[−] (B, top) & equatorial-CN[−] (C, top) form. The calculated Mulliken charges are mentioned with chem draws of the respective figures at bottom.

Table 3 Computationally determined structural and spectroscopic parameters for axial-CN[−] and equatorial-CN[−] geometrical conformers of complex 1 and the experimentally obtained values

Structure	Bond length (Å)				IR stretching (cm ^{−1})	
	Fe-CO	Fe-CN	Fe-Fe	Fe-S	ν_{CO}	ν_{CN}
axial-CN [−] (4B)	1.74 (CO _t) 1.80, 2.11 (CO _b)	1.90	2.57	2.35	1840, 1934, 1965, 1979, 2015	2102
Equatorial-CN [−] (4C)	1.74	1.90	2.51	2.29	1928, 1946, 1962, 1978, 2020	2114
1 ^a	1.74 ^b	1.88 ^b	2.49 ^b	2.28 ^b	1922 ^c , 1950 ^c , 1960 ^c , 1982 ^c , 2033 ^c	2093 ^c
<i>p</i> -BrC ₆ H ₄ N(CH ₂ S) ₂ Fe ₂ CO ₆ (4A)	1.79 ^d	NA	2.50 ^d	2.26 ^d	1999 ^c , 2038 ^c , 2076 ^c	NA
	1.77	NA	2.48	2.29	2005, 2032, 2066	

^a The synthesized complex 1. ^b Values were obtained from EXAFS data. ^c Experimentally obtained IR stretching frequencies in CH₃CN solution.

^d Values were obtained from XRD data.

with the experimentally observed spectrum of complex 1 (Fig. 1A, red). Thus, based on the concurrence between the experimental data and the DFT calculated structure and vibrational properties we conclude that the -equatorial conformer of complex 1 (Fig. 4C) is the dominating species in solution.

The calculated Mulliken charges indicate that the -CO ligands in the precursor Fe₂S₂(CO)₆(CH₂)₂NPhBr complex (Fig. 4A) bears overall negative charge suggesting that there is significant back bonding from the occupied orbitals into the unoccupied CO π^* orbitals. On -CN[−] incorporation (*i.e.* -axial- and equatorial-CN[−]) the amount of negative charge delocalized into the -CO ligands increase. This implies stronger back donation into the -CO π^* orbitals when CN[−] ligand is introduced. The total charge on the CN[−] ligand is −0.377 and −0.375 for -axial- and -equatorial-CN[−], respectively, indicating that most of the negative charge of the CN[−] ligand is shifted into the cluster; mostly into the -CO ligands (Fig. 4B and C) as suggested by lowering of ν_{CO} vibrations in complex 1 relative to the precursor complex observed experimentally (Fig. 1A). Note that the Mulliken charge on the bridgehead N atom remains unaltered.

Electrocatalytic reduction of proton in aqueous medium under heterogeneous conditions on EPG

Electrocatalytic H₂ evolution (HER) under heterogeneous condition. The electrode for heterogeneous electrochemical investigations was prepared by drop casting complex 1 on edge plane graphite (EPG) electrode. XPS data of the modified EPG surface showed Fe 2p_{3/2} and 2p_{1/2} transitions (Fig. S2†) at 710.9 eV and 724.5 eV, respectively. These values are typical for binuclear [Fe₂S₂]-H₂ase models.⁷⁰ The nitrogen 1s region (Fig. S2†) showed three components at 397.7 eV, 399.2 eV and 400.5 eV corresponding to the cyanide, amine and the tetraalkylammonium counter cation, respectively.⁸⁹ Presence of thiolate sulphur is evidenced by the S 2p at 163–164 eV (Fig. S2†).

In aqueous solvent CV data indicate that the reduction of complex 1, upon immobilization onto EPG electrode, is observed at −0.35 V *vs.* NHE (Fig. 5A, red dashed line). This redox event is attributed to the Fe(1)–Fe(1)/Fe(1)–Fe(0) process and the area under the CV response indicate $2.25 \pm 0.25 \times 10^{-12}$ mol cm^{−2} electrochemically active complex 1 present on the EPG. Note that while the Fe(1)–Fe(1)/Fe(1)–Fe(0) is −0.76 V in an organic solvent like CH₃CN (Fig. 5A, red), it is demonstrated to shift to considerable higher potentials at −0.35 V *vs.* NHE (Fig. 5A, dashed red) in aqueous medium due to enhanced

solvation of the negatively charged species produced upon reduction by water as was observed for the precursor complex.^{70,90} Electrocatalytic hydrogen evolution (HER) by immobilized **1** was investigated in aq. H_2SO_4 solution by linear sweep voltammetry (LSV). Subsequently, rotating ring disk electrochemistry (RRDE) set up fitted with a Pt-ring encircling the working EPG electrode allowed us *in situ* detection of the hydrogen,⁹¹ produced by the working electrode on sweeping from positive to negative potential. In 0.002 N H_2SO_4 (pH \sim 2.7) solutions, scanning from 0.2 V to -0.8 V with scan rate 50 mV s $^{-1}$ at 300 rpm rotation speed, a large catalytic current was observed with an onset at -0.3 V ($I_{\text{cat}} = 100$ μA) and it reached to a maximum value at -0.65 V (Fig. 5B, red). The hydrogen production was concomitantly detected by the Pt-ring, held at a constant potential 0.7 V where it re-oxidized the H_2 , produced by the working electrode and radially diffuses out to this encircling Pt ring, to H^+ generating an oxidation current (Fig. 5B, red dashed line).⁹¹ No such catalytic current was observed on a bare EPG electrode under identical condition (Fig. 5B, purple). This indicates electrocatalytic hydrogen production by complex **1**. For further confirmation, controlled potential electrolysis (CPE) was performed at -0.4 V vs. NHE in a gas tight two compartment water jacketed cell and the produced gases were characterized by the head space analysis of the cathodic compartment in gas chromatography fitted with thermal conductivity detector (GC-TCD) where H_2 was identified (Fig. 5B, inset, green trace). The HER activity of **1** was compared

with its precursor complex *p*-BrC₆H₄N(CH₂S)₂Fe₂CO₆ *i.e.*, without a CN⁻ ligand. The LSV data (Fig. 5C, red) indicate that **1** catalyses HER with 350 mV lower onset potential than the precursor complex in 0.002 N H_2SO_4 solution (Fig. 5C, olive green). This is because while **1** catalyses HER from its Fe(i)-Fe(0) state, the precursor *p*-BrC₆H₄N(CH₂S)₂Fe₂CO₆ complex catalyzes HER from its Fe(0)-Fe(0) state. Thus, inclusion of CN⁻ leads to higher pK_a of the cluster such that the one electron reduced Fe(i)-Fe(0) state can be protonated and reduction to the two electron reduced Fe(0)-Fe(0) state can be avoided.

To characterize the catalytic ability of complex **1** turn over number (TON), turn over frequency (TOF), faradaic yield (FY) and overpotential (η) of HER are determined. The FY for HER was determined by performing controlled potential electrolysis (CPE) at -0.4 V vs. NHE in 0.1 N H_2SO_4 (Fig. S6A, red†). Over a period of 1 hour, 9.43 C charge had been dispensed from the electrode (*i.e.*, 9.7×10^{-5} moles) and concurrently \sim 1 ml H_2 gas was evolved during CPE. From these results, the FY is determined to be $92 \pm 7\%$. No significant current was observed when bare EPG disc was tested under similar conditions (Fig. S6A,† green). Thus, the TON calculated for this catalyst during CPE is $> 10^7$ and the average TOF is \sim 2230 s $^{-1}$ at pH 1. This is very close to the value of \sim 4000 s $^{-1}$ determined from $I_{\text{cat}}/[\tau]$ (ratio of catalytic current and CV current) experiments in 0.1 N of $[\text{H}^+]$ (Fig. 6A). The η of HER is determined from LSV data at 0.002 N $[\text{H}^+]$. The standard potential for H_2/H^+ couple at this proton concentration is -0.16 V whereas onset of HER ($I_{\text{cat}} = 100$ μA ,

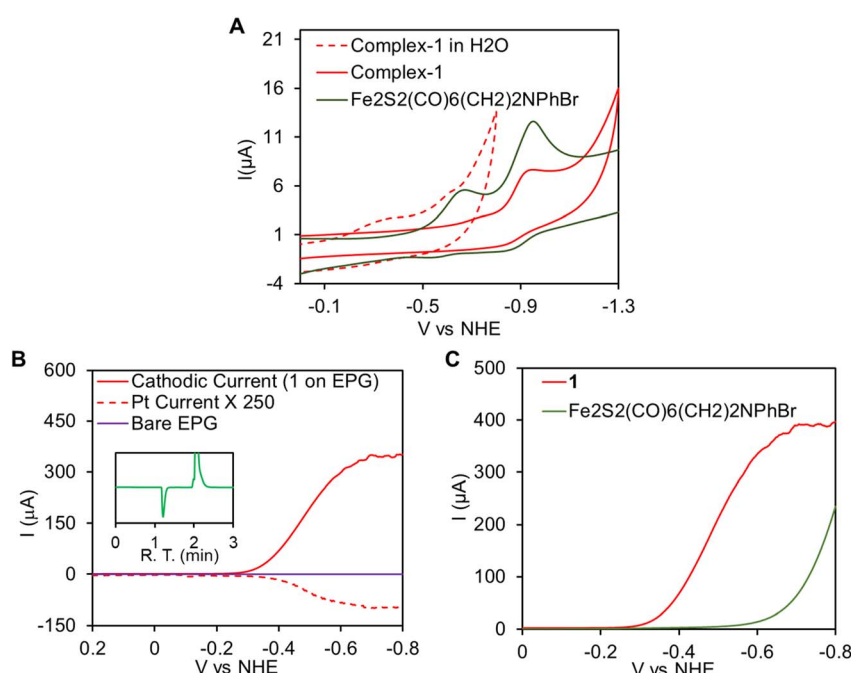


Fig. 5 (A) Overlay of the CV traces of complex **1** (red) and its precursor *p*-BrC₆H₄N(CH₂S)₂Fe₂CO₆ complex in acetonitrile medium (olive green) under homogeneous conditions. The CV of complex **1** immobilized on EPG in aqueous medium is shown in red dashed line. (B) RRDE with complex **1** immobilized on EPG working electrode (red line, indicating electrocatalytic H^+ reduction) which is swept from 0.2 V to -0.8 V and the corresponding Pt-ring current (red dashed line, indicating H_2 oxidation *i.e.*, detection) with the ring held at a constant potential of 0.7 V in aqueous 0.002 N H_2SO_4 . Bare EPG trace is shown in purple, inset gas chromatogram of the headspace gas analysis after CPE of complex **1** immobilized on EPG at -0.4 V vs. NHE in 0.1 N H_2SO_4 . (C) Overlay of the LSV traces for complex **1** (red) and *p*-BrC₆H₄N(CH₂S)₂Fe₂CO₆ (Olive green) on EPG.



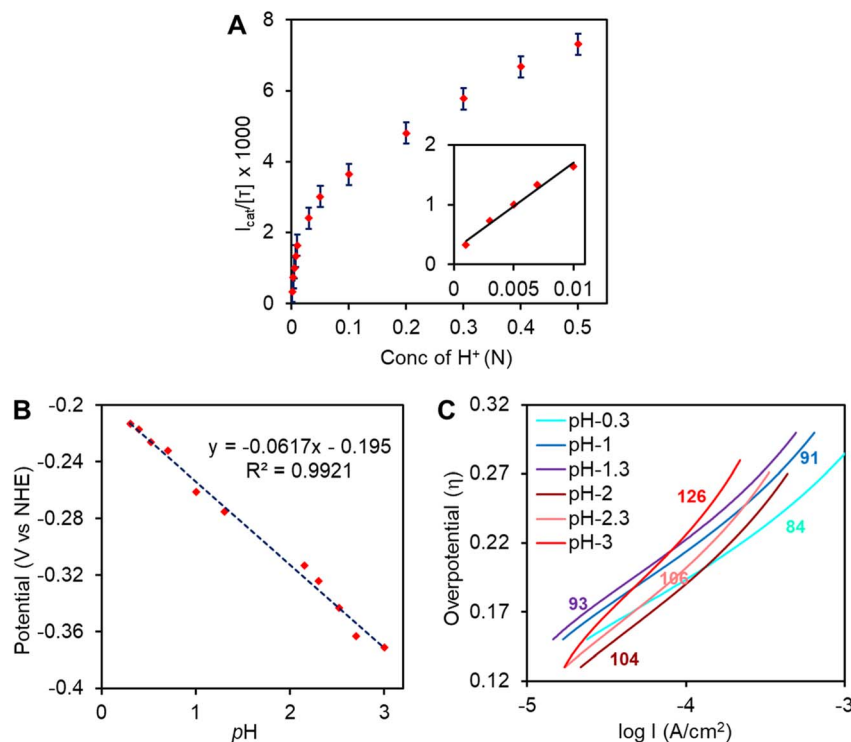


Fig. 6 (A) Plot of $I_{\text{cat}}/[\tau]$ at varying acid concentrations of complex **1** on EPG. I_{cat} values were recorded at -0.5 V vs. NHE for each $[\text{H}^+]$, inset plot of $I_{\text{cat}}/[\tau]$ at lower acid concentrations. (B) Onset potential (V vs. NHE) @ $I_{\text{cat}} = 100$ μA vs. pH plot. (C) Tafel plots at different pHs. The values are the Tafel slopes at different pHs and reported in mV dec⁻¹.

area of electrode ~ 0.1 cm^2 *i.e.* $j_{\text{cat}} = 1$ mA cm^{-2} where j is the exchange current density) is -0.4 V. Hence, the onset overpotential is only about 0.24 V, which is one of the lowest overpotential for HER to be reported so far for any $[\text{Fe}-\text{Fe}]$ H_2O inspired molecular catalyst in aqueous medium. The XPS data (Fig. S2†) and the ATR-IR (Fig. S6B†) data of the graphite electrode were collected after CPE and showed that the catalyst was stable over the CPE time scale. This is also implied by the constant slope of the current during CPE.

Mechanistic considerations

Effect of acid concentrations. By varying bulk H^+ concentration over a range of 0.001 N– 0.5 N $[\text{H}^+]$ (pH 3–pH 0.3), a sharp increase of the catalytic current was observed (Fig. S3†) and reached to a maximum $I_{\text{cat}}/[\tau]$ value (*i.e.*, TOF) of 7300 s^{-1} at 0.5 N H_2SO_4 (Fig. 6A). The saturation of I_{cat} at high acid concentration may not reflect saturation of catalytic activity as the catalysis is retarded by bubble accumulation (H_2 gas, Fig. S9†) on the rotating electrode (even at 2000 rpm rotation rate) at high proton concentrations. This 7300 s^{-1} TOF value remains almost unchanged over consecutive 50 scans at 0.5 N H_2SO_4 (Fig. S4†). At lower acid concentrations (Fig. 6A, inset), where bubbles do not accumulate on the rotating electrode, the $I_{\text{cat}}/[\tau]$ value linearly increased with the $[\text{H}^+]$, indicating pseudo 1st order kinetics of HER. Note that the (i_{cat}/τ) of the hydrogen production ~ 300 s^{-1} at 0.001 N H_2SO_4 *i.e.*, at pH = 3. The onset potential ($I_{\text{cat}} = 100$ μA) for the faradaic current showed a positive shift with a slope of 60

± 2 mV per unit change in pH of the solution (Fig. 6B). These two observations suggest $1\text{e}^-/1\text{H}^+$ proton coupled electron transfer is involved in rate determining step. Further analysis of the LSV currents at low current range showed different slopes in $\log I$ vs. η plots (Tafel plot) at different pHs (Fig. 6C). At higher pHs, a slope of 126 mV dec⁻¹ was obtained while a gradual decrease of the slope up to 84 mV dec⁻¹ was attained at lower pHs (pH = 0.3). The decrease in slope value can be attributed to bubble formation encountered or some side reaction at higher acid concentrations. Notably, a 120 mV dec⁻¹ slope is expected for a metal-hydride formation rate determining step according to pure Volmer kinetic mechanism.^{92–94} Overall a PCET step for di-iron hydride, $[\text{Fe}(\text{i})-\text{Fe}(\text{ii})]-\text{H}$, formation is proposed as rate determining step for this catalysis by complex **1**. Unfortunately, no evidence for the formation of this species during heterogeneous catalysis on the EPG electrode can be provided but evidence for the formation of this species is provided using FTIR-SEC under homogeneous conditions (*vide infra*).

Kinetic analyses

Koutecky-Levich analysis. Complex **1** reduces H^+ at diffusion-controlled limit at low $[\text{H}^+]$ with overpotential of 0.24 V. The diffusion limited current has two components–

$$I_{\text{cat}}^{-1} = i_{\text{K}}(E)^{-1} + i_{\text{L}}^{-1}$$

Where $i_{\text{K}}(E)$ is the potential dependent kinetic current and i_{L} is the Levich current which is given by,

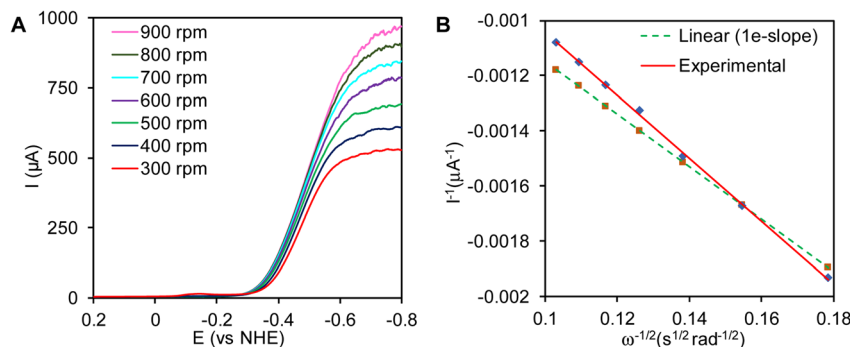


Fig. 7 (A) Plot of linear sweep voltammetry (LSV) with increasing rotation rates scanning from 0.2 V to -0.8 V in 0.005 N H_2SO_4 solution. (B) Plot of the $(1/I_{\text{cat}})$ vs. $1/\omega^{1/2}$ where catalytic current (I_{cat}) measured at -0.6 V.

$$i_L = 0.62nFA[\text{H}^+](D_{\text{H}^+})^{2/3}\omega^{1/2}\nu^{-1/6}$$

where n is the number of electrons transferred to the substrate, A is the area of the disc (0.096 cm^2), $[\text{H}^+]$ is the concentration of H^+ i.e., 0.005 N , D_{H^+} is the diffusion coefficient of H^+ ($9.3 \times 10^{-5} \text{ cm}^2 \text{ s}^{-1}$), ω is the angular velocity of the disc and ν is the kinematic viscosity of the solution ($0.01 \text{ cm}^2 \text{ s}^{-1}$).

The plot of inverse of catalytic current, at -0.6 V vs. NHE where the current is mass transfer controlled, varied linearly with the inverse of the square root of the angular rotation rates (Fig. 7A). The plot of I^{-1} vs. $\omega^{-1/2}$ was linear and the slope obtained from the experimental results was similar to the predicted slope for $1e^-$ reduction process (Fig. 7B). This indicates that complex **1** reduces the H^+ , by one electron to $1/2 \text{ H}_2$, i.e., $\text{H}^+ + \text{e}^- \rightarrow 1/2 \text{ H}_2$

The potential dependent current $i_K(E)$ is obtained from the inverse of the intercept of the K-L plot and is expressed as,

$$I_K(E) = k[\text{H}^+]nF[A][\tau][\text{H}^+]$$

where $k_{[\text{H}^+]}$ is the 2nd order rate constant for H^+ reduction, $[\tau]$ is the number of molecules of **1** on the electrode, $[A]$ is the macroscopic area of the electrode and n, F and $[\text{H}^+]$ has their usual meanings. The second order rate of proton reduction has been calculated to be $\sim 2.5 \pm 0.2 \times 10^{11} \text{ M}^{-1} \text{ s}^{-1}$.

In the absence of *in situ* spectroscopic methods amenable to probe a catalyst heterogenized on graphite electrodes in *operando*, HER in organic solvents was investigated with the goal of identifying potential intermediates involved in HER using IR-SEC.

CV under homogenous condition. Cyclic voltammetry (CV) of a solution of complex **1** in CH_3CN showed a peak (E_{red}) centred at -0.76 V with peak-to-peak separation (ΔE_p) of 120 mV (Fig. 5A, red). This represents the reduction of the Fe(i)-Fe(i) state to the Fe(i)-Fe(0) state as demonstrated for similar synthetic models.⁹⁵ The $\text{Fe(i)-Fe(i)/Fe(i)-Fe(0)}$ process is lowered by 140 mV relative to that of the precursor $p\text{-BrC}_6\text{H}_4\text{N}(\text{CH}_2\text{S})_2\text{-Fe}_2\text{CO}_6$ complex due to ligation of an anionic CN^- ligand.

A catalytic current at similar potential was observed (Fig. 8A, blue line) in the presence of 2 equivalents of *p*-toluenesulfonic acid (*p*TsOH, $pK_a \approx 8.3$ in CH_3CN)⁹⁶ and the catalytic current increases significantly with sequential addition of *p*TsOH. The sharp increase in its current intensity indicates that complex **1** has the ability for the electrocatalytic reduction of protons to H_2 . To confirm this controlled potential electrolysis (CPE) was performed at -0.9 V vs. NHE of the 0.3 mM acetonitrile solution of complex **1** in the presence of 80 equivalent of *p*-toluenesulfonic acid (*p*TsOH) (Fig. 9A). The headspace gas analysis by GC-TCD confirmed the produced gas to be H_2 (Fig. 8B, red

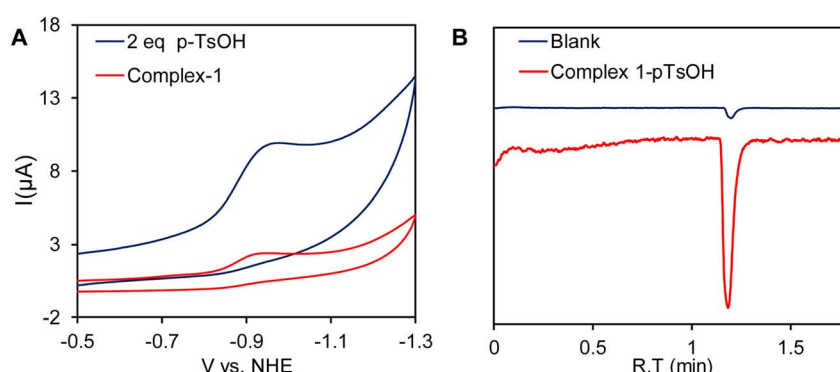


Fig. 8 (A) Cyclic voltammogram of complex **1** in CH_3CN (red line) and in the presence of *p*-toluenesulfonic acid (*p*TsOH) (blue line) under homogeneous conditions. (B) Gas chromatogram of the headspace gas analysis after CPE of complex **1** in the presence of 80 equivalent of *p*TsOH in CH_3CN medium (red trace). The experiment was also repeated with blank electrodes under similar conditions (blue trace).

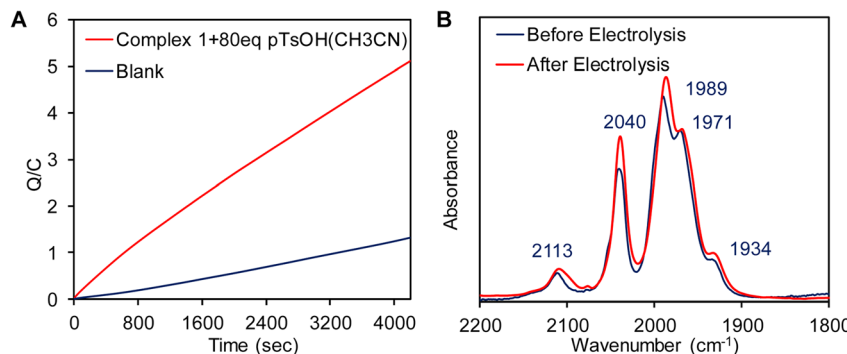


Fig. 9 (A) Overlay of controlled potential bulk electrolysis with the complex 1 at -0.9 V vs. NHE in CH_3CN medium in the presence of 80 equivalent of $p\text{TsOH}$ (red line) and without complex 1 (blue line) under identical conditions. (B) FT-IR of the of complex 1 before and after bulk electrolysis in the presence of $p\text{TsOH}$.

trace). During the CPE 5.12 C charge was consumed over the course of 70 min (Fig. 9A) and 0.5 ml of H_2 was evolved. From these results, the FY was determined to be 84% and the TON was calculated to be 15. In the absence of the catalyst no significant amount of H_2 was produced under similar condition (Fig. 8B, blue trace). The FTIR spectra recorded before and after the CPE experiment confirmed that the catalyst is stable and also the CN^- ligands are not protonated under these conditions as has been reported for di-cyano complexes (Fig. 9B).³⁴

FTIR-SEC. The resting state of complex 1 is likely a *trans*- $\text{Fe}(\text{i})-\text{Fe}(\text{i})$ configuration; a conclusion drawn from the agreement of its vibrational frequencies to those obtained through DFT calculations (Table 4) and EXAFS data (Table 3). Upon the addition of 1 equivalent *p*-toluenesulfonic acid (*p*TsOH), notable changes were observed in the vibrational spectra of complex 1. Specifically, all frequencies associated with carbonyl and cyanide groups were blue shifted to higher wavenumbers by $\approx 10-20$ cm^{-1} (Fig. 11A, blue line). Based on previous reports we can conclude that the magnitude of the shift is similar to the result observed upon protonation of neutral -ADT bridged complex with strong acid and characteristic for protonation of the bridgehead nitrogen (Fig. 11A).^{97,98} Thus, the CN^- ligand is not protonated in the presence of *p*TsOH and this is likely because of the delocalization of the electron density of the CN^- into the cluster as indicated by FTIR data and DFT calculations of this complex. DFT calculations also support the observed blue shift in the ν_{CO} vibrations (Fig. 11C and Table 4). To further probe and characterize the intermediates that arise during the catalytic cycle, we conducted FTIR spectro-electrochemistry (IR-

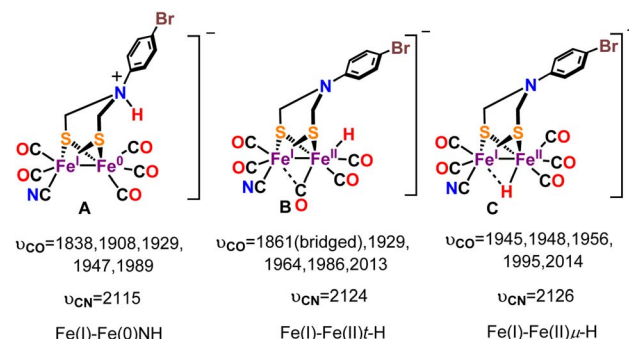


Fig. 10 Probable one electron reduced protonated species and their computed ν_{CO} and ν_{CN} vibrational frequencies.

SEC) experiment. We subjected the N-protonated form of complex 1 (Complex 1 + 1 eq. *p*TsOH) to electrochemical reduction by performing controlled potential electrochemistry (CPE) at -0.9 V vs. NHE, within a conventional OTTLE cell to probe the mechanism of HER.

Reduction of complex 1 in the presence of 1 equivalent *p*TsOH did not result in red shift in the ν_{CO} and ν_{CN} vibrations (Fig. 11B, blue line) as would be expected for a reduction event in the cluster which would have increased back bonding to carbonyl and cyanide ligands. For example, reduction of the $\text{Fe}(\text{i})-\text{Fe}(\text{i})$ of a ADT bound $\text{Fe}_2(\text{CO})_6$ cluster accompanied with protonation of the ADT nitrogen is associated with >100 cm^{-1} red shift in the ν_{CO} .⁹⁹ Specifically, one of the ν_{CO} vibrations red shifted significantly to 1876 cm^{-1} which is much lower than the

Table 4 Experimental and theoretical vibrational frequencies of different species involved in catalytic cycle

Complex	IR stretching frequencies (cm^{-1})			
	Experimental (In CH_3CN)		Theoretical (BP86)	
	ν_{CN}	ν_{CO}	ν_{CN}	ν_{CO}
Complex 1 [$\text{Fe}(\text{i})-\text{Fe}(\text{i})$]	2093	2033, 1982, 1960, 1950, 1922	2114	2020, 1978, 1962, 1946, 1928
Complex 1 + <i>p</i> TsOH [$\text{Fe}(\text{i})-\text{Fe}(\text{i})\text{NH}$] ⁺	2113	2040, 1989, 1971, 1961, 1934	2127	2042, 2009, 1989, 1962, 1955
Complex 1 + <i>p</i> TsOH + (e^-) [$\text{Fe}(\text{i})-\text{Fe}(\text{n})\text{t-H}$]	2095	2036, 1976, 1950, 1923, 1876	2124	2013, 1986, 1964, 1929, 1861
Complex 1 + <i>p</i> TsOD + (e^-) [$\text{Fe}(\text{i})-\text{Fe}(\text{n})\text{t-D}$]	2095	2036, 1974, 1950, 1925, 1860	2124	2013, 1986, 1964, 1929, 1852



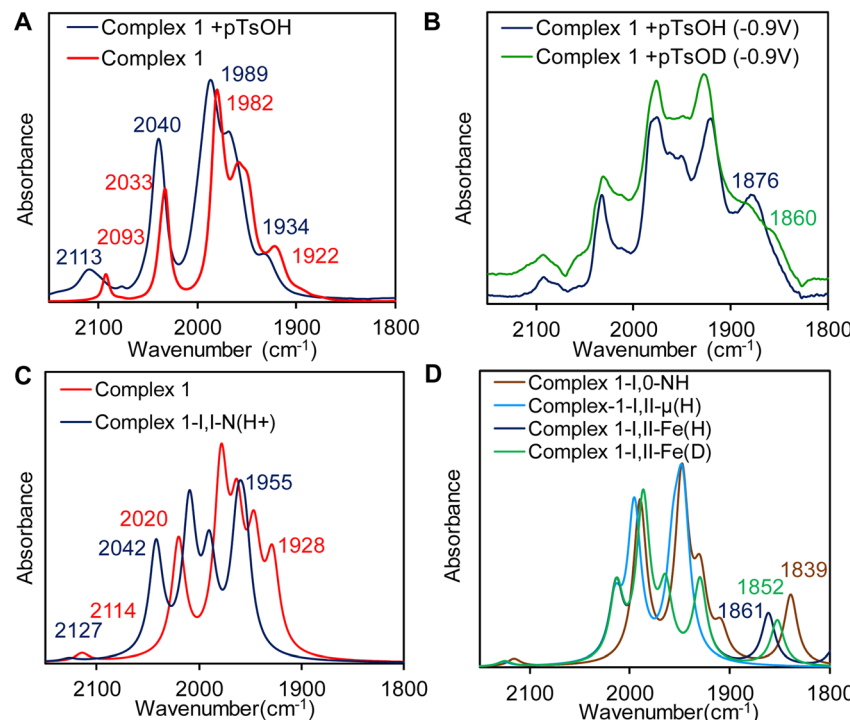


Fig. 11 (A) FTIR spectra of complex 1 (red line) and complex 1 in the presence of 1 equivalent *p*TsOH (blue line). (B) IR-SEC data of complex 1 @ -0.9 V vs. NHE in the presence of *p*TsOH (blue line) and *p*TsOD (green line). (C) Computed vibrations of complex 1 (red line) and complex 1 in the presence of 1 equivalent of *p*TsOH (blue line) and *p*TsOD (green line). (D) Computed vibrations of model A (orange line), B (dark blue line) and C (blue line) (Fig. 10) and the deuterated form of model B (green line).

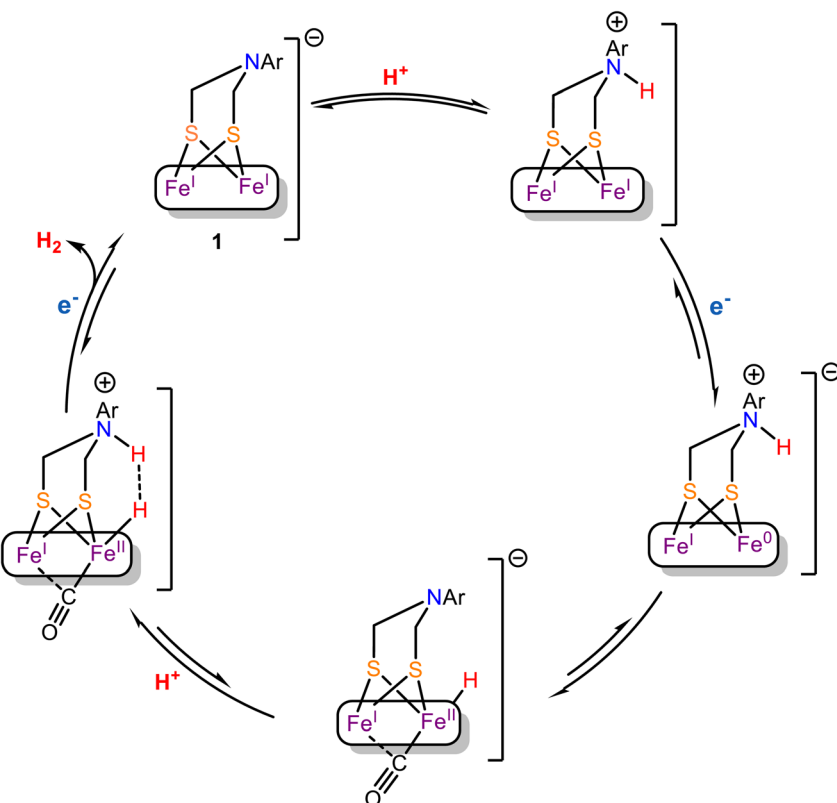
other terminal ν_{CO} vibrations and would be consistent with a μCO formation during reduction in the presence of H^+ source. Furthermore, the peak at 1876 cm^{-1} (Fig. 11B, blue line) appears to shift to 1860 cm^{-1} (Fig. 11B, green line) when *p*TsOD was used as a D^+ source *i.e.*, this ν_{CO} shows a H/D isotope effect. Note that a $\text{Fe}-\text{H}$ vibration is expected to show a H/D isotope shift $>570\text{ cm}^{-1}$ using simple harmonic oscillator approximation. Similarly, H/D shifts associated with hydrogen bonding to $-\text{CO}$ ligands are very small.¹⁰⁰ The shift observed here is 16 cm^{-1} which suggests that the species produced in IR-SEC is likely to be a metal hydride species where a ν_{CO} coupled to a $\nu_{\text{Fe}-\text{H}}$. Similar shift of a $\mu\text{-CO}$ due to coupling with a terminal hydride trans to it in $[\text{Fe}-\text{Fe}] \text{H}_2$ ases.²⁷ There is some residual 1876 cm^{-1} peak in the deuterated solvent from residual H_2O in the electrolyte.

DFT calculations on possible structure of the intermediate. DFT calculations provided a valuable insight into the nature of this one electron reduced protonated species. Three different one electron reduced protonated species may be formed during the catalytic cycle. They include models with ADT protonated and cluster reduced for $\text{Fe}(\text{i})-\text{Fe}(\text{0})$ state (Fig. 10A, $\text{Fe}(\text{i})-\text{Fe}(\text{0})\text{NH}$), a model which is reduced by one electron and protonated at the Fe to result in a *t*-H (Fig. 10B, $\text{Fe}(\text{i})-\text{Fe}(\text{ii})\text{t-H}$), a model which is reduced by one electron and protonated to result in a $\mu\text{-H}$ (Fig. 10C, $\text{Fe}(\text{i})-\text{Fe}(\text{ii})\mu\text{-H}$) and their computed $-\nu_{\text{CO}}$ and $-\nu_{\text{CN}}$ vibrational stretching frequencies are also indicated. Note that only the equatorial conformation is considered in these calculations. The experimental vibrations match well with computed

vibrations of the $\text{Fe}(\text{i})-\text{Fe}(\text{ii})\text{t-H}$ species, containing a terminal hydride (*t*-H, Fig. 11B and D). One of the $-\text{CO}$ moves to a semi-bridging position (*i.e.*, $\mu\text{-CO}$) resulting in a substantial weakening of its $\mu\text{-CO}$ relative to those of the terminal CO's. This $\mu\text{-CO}$ is trans to the *t*-H (Fig. 10B) resulting in mixing of the ν_{CO} and $\nu_{\text{Fe}-\text{H}}$ which results in the shift of the ν_{CO} at 1861 cm^{-1} to 1852 cm^{-1} when the *t*-H is replaced by *t*-D in these calculations (Fig. 11C). The $\text{Fe}(\text{i})-\text{Fe}(\text{ii})\mu\text{-H}$ model (Fig. 10C) which does not have a $\mu\text{-CO}$ cannot explain the weak ν_{CO} observed at 1876 cm^{-1} and the $\text{Fe}(\text{i})-\text{Fe}(\text{0})\text{NH}$ model (Fig. 10A) does not couple to ν_{CO} and hence does not show a H/D effect on it as observed. Thus, the computed models bearing the $\mu\text{-H}$ and NH do not show any H/D isotope sensitive vibration in this region. The computed vibrations for doubly protonated species blue shift significantly from the experimental data and were eliminated from consideration (Fig. S7 and S8B†). The results obtained from the IR-SEC and DFT calculation suggest that (a) the reduced species bears a $\mu\text{-CO}$ ligand and (b) the proton vibration is involved in the 1876 cm^{-1} ν_{CO} mode which is likely to occur is the hydride is trans to the $\mu\text{-CO}$ ligand. The H/D isotopic shift of this 1876 cm^{-1} vibration observed experimentally which is also present in the computational model supports this proposal.

Discussion

The EXAFS, Mössbauer and FTIR data of complex 1 is consistent with the presence of terminal cyanide ligand. Thus, along with the $\mu\text{-ADT}$ and the terminal CN^- ligand, this model is a close



Scheme 3 Proposed mechanistic pathway for HER catalyzed by complex 1.

structural analogue of the active site of the [Fe–Fe] H₂ases. The presence of the CN[−] raises the basicity of the cluster in **1** such that HER current of the CN[−] bound form at higher pH is remarkably higher relative to the precursor complex. Under aqueous conditions, the 1st order dependence of the rate with [H⁺] at low acid concentrations suggest that binding of H⁺ is involved in rate determining step (rds). The 62 mV/pH slope of the pH *vs.* onset potential plot (Fig. 6B) suggest that proton coupled electron transfer (PCET) is operating at the potential determining step in the kinetic region.^{101,102} Now, protonation could occur either at the bridgehead N to generate reduced N-protonated species or at the reduced Fe-centre to form a Fe–H species (terminal or bridging).¹⁰³ The Tafel slope is determined to be 126 mV dec^{−1} which is close to the value expected for Volmer mechanism implying the involvement of a Fe–H species in the rds.^{92–94} In an organic solvent (CH₃CN), under homogeneous conditions, complex **1** catalyze HER at −0.9 V *vs.* NHE (Fig. 8A) and remains stable during CPE for more than an hour (Fig. 9). *In situ* FTIR-SEC provide preliminary evidence for a terminal hydride [Fe(I)–Fe(II)–H] with a μ-CO during catalysis when the ν_{CO} shifts on deuteration due to coupling with a t-H in a fashion similar to that observed for [Fe–Fe] H₂ase.²⁷ The accumulation of the hydride species during HER in organic medium implies that its further protonation is likely the rds which is in line with the suggestions from Tafel slope obtained under aqueous conditions. However, the solvation energies of species involved in catalysis will be very different in aqueous and organic solvents and the mechanism may vary. To rationalize the sequence of

events, we proposed that the mechanistic pathway proposed by Rauchfuss is at play here (Scheme 3) *i.e.* (i) In the presence of *p*TsOH, the complex **1** forms a N-protonated complex, (ii) the N-protonated complex **1** undergoes a one-electron reduction under electrochemical condition along with an intramolecular proton transfer from the bridge head nitrogen atom to the reduced Fe(I)–Fe(0) center to form the –CO bridged Fe(I)–Fe(II)t-H species. This step may be mediated by Fe(I)–Fe(0)NH species but the isomerization of it to Fe(I)–Fe(II)t-H may be too rapid to be observed in IR-SEC. (iii) The protonation of the [Fe(I)–Fe(II)–H] species in the rds then leads to H₂ evolution.

The CN[−] bound complex **1** exhibits the Fe(I)–Fe(I)/Fe(I)–Fe(0) E_{1/2} at −0.76 V in acetonitrile which is 140 mV more cathodic than the E_{1/2} for the same process of the neutral precursor *p*-BrC₆H₄N(CH₂S)₂Fe₂CO₆ complex; understandably the negative charge of the complex **1** shifted its E_{1/2} to more cathodic potential relative to its neutral precursor. However, complex **1** shows an onset for HER at ∼350 mV more positive potential in aqueous medium and exhibits significantly greater HER current at −0.5 V when compared to its precursor complex (Fig. 5C). The greater reactivity for HER of complex **1** result from the fact that its Fe(I)–Fe(0) state is active while for the precursor *p*-BrC₆H₄N(CH₂S)₂–Fe₂CO₆ complex Fe(0)–Fe(0) state is active at these low acid concentrations. At a given potential (−0.5 V *vs.* NHE), the HER current is 10^{3–4} times larger for complex **1** relative to its precursor at higher pHs (Fig. S5†). Thus, due to the presence of an anionic CN[−] ligand, the electron density of the Fe(I)–Fe(0) state of complex **1**, is high enough to allow protonation of the Fe center.

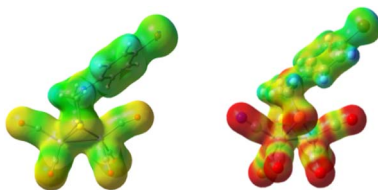


Fig. 12 Electrostatic potential plots of the precursor-*p*-BrC₆H₄-N(CH₂S)₂Fe₂(CO)₆ (left) and complex 1 (right).

A pertinent concern of employing a CN[−] ligand bound to an apparently weak Lewis acid, the reduced [Fe–Fe] cluster, under acidic conditions is the possibility of losing it *via* protonation.³⁴ Both the XPS and IR data acquired before and after 1 h of electrolysis indicates that the ratio of carbonyl and CN[−] peaks remain constant *i.e.*, CN[−] ligands are not preferentially protonated. This is since the electron density of the CN[−] ligand is strongly delocalized into the cluster due to the presence of the π accepting -CO ligands (Fig. 12, right). Similar stabilization of anionic ligand binding to a formally weak Lewis acid centre has been proposed for [Fe–Fe] H₂ase and encountered in the mononuclear iron active site in Hmd where the -CO and acyl ligands facilitated the delocalization of the electron density of anionic ligands into the active site enhancing their binding affinities.^{1,76,104} The synthetic [Fe–Fe] clusters with terminal CN[−] ligand which were reported to decompose in the presence of acid had at least one of the terminal CO's replaced by weaker π acceptors like phosphine or CN[−] weakening the charge delocalization.³⁴ Furthermore, the data obtained from both under aqueous and organic conditions indicate that protonation upon reduction forming the terminal Fe(i)–Fe(ii)-H species with a μ-CO is extremely fast occurring at diffusion controlled rates in aqueous medium. This minimizes the lifetime of Fe(i)–Fe(0) species during catalysis minimizing the possibility of CN[−] protonolysis during catalysis.

Conclusions

In summary, a synthetic model of the [Fe–Fe] H₂ase bearing ADT and CN[−] terminal ligands is reported. The presence of CN[−] raises the pK_a of the cluster allowing HER at mildly acidic pHs at extremely facile diffusion limited rates in aqueous medium. The electron donation from the CN[−] ligand enables the cluster to catalyze HER from its Fe(i)–Fe(0) state which results in a substantial lowering of overpotential associated with HER catalyzed by similar complexes but without the CN[−] ligand as these need to be reduced to their Fe(0)–Fe(0) states for them to be able to catalyze HER. *In situ* FTIR-SEC suggest the formation of a terminal hydride species *via* one electron reduction and protonation of the Fe(i)–Fe(i) cluster. Importantly, the CN[−] ligand is found to remain stable during these experiments.

Data availability

All data associated with this publication are provided in the ESI.†

Author contributions

A. N. synthesized the complex and performed characterization of the complex. A. N. and S. D. carried out electrochemical experiments and spectroscopic studies. S. P. and A. N. has performed the IR-SEC experiment. A. R. assisted in DFT-calculations. P. S., S. G. and S. P. recorded the EXAFS data. S. G. D. supervised the work and assisted in the data analysis. A. D. D. designed the project, assisted in the data analysis wrote the manuscript.

Conflicts of interest

There are no conflicts to declare.

Acknowledgements

A. N. thanks IACS for fellowship. S. P. acknowledge CSIR-SRF for fellowship. This work is funded by Department of Science and Technology, India, (DST/TMD/HFC/2K18/90) (A.D.), the US National Institutes of Health grant GM65440 (SPC) and the US DOE OBER (SPC). All X-ray spectroscopy was performed at the Stanford Synchrotron Radiation Light source (SSRL), a national user facility operated by Stanford University on behalf of the DOE OBES. The SSRL Structural Molecular Biology Program is supported by the DOE OBER, and the NIH, National Center for Research Resources, Biomedical Technology Program.

References

- 1 S. Dey, P. K. Das and A. Dey, *Coord. Chem. Rev.*, 2013, **257**, 42–63.
- 2 R. K. Thauer, A. R. Klein and G. C. Hartmann, *Chem. Rev.*, 1996, **96**, 3031–3042.
- 3 P. M. Vignais and B. Billoud, *Chem. Rev.*, 2007, **107**, 4206–4272.
- 4 J. C. Fontecilla-Camps, A. Volbeda, C. Cavazza and Y. Nicolet, *Chem. Rev.*, 2007, **107**, 4273–4303.
- 5 S. Shima and R. K. Thauer, *Chem. Rec.*, 2007, **7**, 37–46.
- 6 S. Rospert, J. Breitung, K. Ma, B. Schwörer, C. Zirngibl, R. K. Thauer, D. Linder, R. Huber and K. O. Stetter, *Arch. Microbiol.*, 1991, **156**, 49–55.
- 7 M. Y. Dahrenbourg, E. J. Lyon, X. Zhao and I. P. Georgakaki, *Proc. Natl. Acad. Sci. U. S. A.*, 2003, **100**, 3683–3688.
- 8 M. Frey, *ChemBioChem*, 2002, **3**, 153–160.
- 9 Y. Nicolet, C. Piras, P. Legrand, C. E. Hatchikian and J. C. Fontecilla-Camps, *Structure*, 1999, **7**, 13–23.
- 10 J. W. Peters, W. N. Lanzilotta, B. J. Lemon and L. C. Seefeldt, *Science*, 1998, **282**, 1853–1858.
- 11 Y. Nicolet, A. L. de Lacey, X. Vernède, V. M. Fernandez, E. C. Hatchikian and J. C. Fontecilla-Camps, *J. Am. Chem. Soc.*, 2001, **123**, 1596–1601.
- 12 W. Lubitz, E. Reijerse and M. van Gastel, *Chem. Rev.*, 2007, **107**, 4331–4365.
- 13 C. V. Popescu and E. Müncck, *J. Am. Chem. Soc.*, 1999, **121**, 7877–7884.



14 A. Adamska, A. Silakov, C. Lambertz, O. Rüdiger, T. Happe, E. Reijerse and W. Lubitz, *Angew. Chem. Int. Ed. Engl.*, 2012, **51**, 11458–11462.

15 C. Lorent, S. Katz, J. Duan, C. J. Kulka, G. Caserta, C. Teutloff, S. Yadav, U.-P. Apfel, M. Winkler, T. Happe, M. Horch and I. Zebger, *J. Am. Chem. Soc.*, 2020, **142**, 5493–5497.

16 M. Haumann and S. T. Stripp, *Acc. Chem. Res.*, 2018, **51**, 1755–1763.

17 C. Sommer, A. Adamska-Venkatesh, K. Pawlak, J. A. Birrell, O. Rüdiger, E. J. Reijerse and W. Lubitz, *J. Am. Chem. Soc.*, 2017, **139**, 1440–1443.

18 M. W. Ratzloff, J. H. Artz, D. W. Mulder, R. T. Collins, T. E. Furtak and P. W. King, *J. Am. Chem. Soc.*, 2018, **140**, 7623–7628.

19 M. L. K. Sanchez, C. Sommer, E. Reijerse, J. A. Birrell, W. Lubitz and R. B. Dyer, *J. Am. Chem. Soc.*, 2019, **141**, 16064–16070.

20 J. A. Birrell, V. Pelmenschikov, N. Mishra, H. Wang, Y. Yoda, K. Tamasaku, T. B. Rauchfuss, S. P. Cramer, W. Lubitz and S. DeBeer, *J. Am. Chem. Soc.*, 2020, **142**, 222–232.

21 P. Rodríguez-Maciá, N. Breuer, S. DeBeer and J. A. Birrell, *ACS Catal.*, 2020, **10**, 13084–13095.

22 P. Rodríguez-Maciá, K. Pawlak, O. Rüdiger, E. J. Reijerse, W. Lubitz and J. A. Birrell, *J. Am. Chem. Soc.*, 2017, **139**, 15122–15134.

23 A. Silakov, B. Wenk, E. Reijerse and W. Lubitz, *Phys. Chem. Chem. Phys.*, 2009, **11**, 6592–6599.

24 D. W. Mulder, Y. Guo, M. W. Ratzloff and P. W. King, *J. Am. Chem. Soc.*, 2017, **139**, 83–86.

25 E. J. Reijerse, C. C. Pham, V. Pelmenschikov, R. Gilbert-Wilson, A. Adamska-Venkatesh, J. F. Siebel, L. B. Gee, Y. Yoda, K. Tamasaku, W. Lubitz, T. B. Rauchfuss and S. P. Cramer, *J. Am. Chem. Soc.*, 2017, **139**, 4306–4309.

26 V. Pelmenschikov, J. A. Birrell, C. C. Pham, N. Mishra, H. Wang, C. Sommer, E. Reijerse, C. P. Richers, K. Tamasaku, Y. Yoda, T. B. Rauchfuss, W. Lubitz and S. P. Cramer, *J. Am. Chem. Soc.*, 2017, **139**, 16894–16902.

27 M. Winkler, M. Senger, J. Duan, J. Esselborn, F. Wittkamp, E. Hofmann, U.-P. Apfel, S. T. Stripp and T. Happe, *Nat. Commun.*, 2017, **8**, 16115.

28 C.-H. Hsieh, Ö. F. Erdem, S. D. Harman, M. L. Singleton, E. Reijerse, W. Lubitz, C. V. Popescu, J. H. Reibenspies, S. M. Brothers, M. B. Hall and M. Y. Daresbourg, *J. Am. Chem. Soc.*, 2012, **134**, 13089–13102.

29 M. T. Olsen, M. Bruschi, L. De Gioia, T. B. Rauchfuss and S. R. Wilson, *J. Am. Chem. Soc.*, 2008, **130**, 12021–12030.

30 A. K. Justice, M. J. Nilges, T. B. Rauchfuss, S. R. Wilson, L. De Gioia and G. Zampella, *J. Am. Chem. Soc.*, 2008, **130**, 5293–5301.

31 A. T. Fiedler and T. C. Brunold, *Inorg. Chem.*, 2005, **44**, 9322–9334.

32 S. Amanullah, P. Saha, A. Nayek, M. E. Ahmed and A. Dey, *Chem. Soc. Rev.*, 2021, **50**, 3755–3823.

33 V. Artero, G. Berggren, M. Atta, G. Caserta, S. Roy, L. Pecqueur and M. Fontecave, *Acc. Chem. Res.*, 2015, **48**, 2380–2387.

34 F. Gloaguen, J. D. Lawrence and T. B. Rauchfuss, *J. Am. Chem. Soc.*, 2001, **123**, 9476–9477.

35 J. T. Kleinhaus, F. Wittkamp, S. Yadav, D. Siegmund and U.-P. Apfel, *Chem. Soc. Rev.*, 2021, **50**, 1668–1784.

36 T. B. Rauchfuss, *Acc. Chem. Res.*, 2015, **48**, 2107–2116.

37 C. Tard and C. J. Pickett, *Chem. Rev.*, 2009, **109**, 2245–2274.

38 T. Liu and M. Y. Daresbourg, *J. Am. Chem. Soc.*, 2007, **129**, 7008–7009.

39 J. M. Camara and T. B. Rauchfuss, *Nat. Chem.*, 2012, **4**, 26–30.

40 F. Gloaguen and T. B. Rauchfuss, *Chem. Soc. Rev.*, 2009, **38**, 100–108.

41 A. Nayek, M. E. Ahmed, S. Samanta, S. Dinda, S. Patra, S. G. Dey and A. Dey, *J. Am. Chem. Soc.*, 2022, **144**, 8402–8429.

42 M. Razavet, S. J. Borg, S. J. George, S. P. Best, S. A. Fairhurst and C. J. Pickett, *Chem. Commun.*, 2002, 700–701.

43 M. E. Carroll, B. E. Barton, T. B. Rauchfuss and P. J. Carroll, *J. Am. Chem. Soc.*, 2012, **134**, 18843–18852.

44 A. Silakov, J. L. Shaw, E. J. Reijerse and W. Lubitz, *J. Am. Chem. Soc.*, 2010, **132**, 17578–17587.

45 O. F. Erdem, L. Schwartz, M. Stein, A. Silakov, S. Kaur-Ghumaan, P. Huang, S. Ott, E. J. Reijerse and W. Lubitz, *Angew. Chem. Int. Ed. Engl.*, 2011, **50**, 1439–1443.

46 H. J. Redman, P. Huang, M. Haumann, M. H. Cheah and G. Berggren, *Dalton Trans.*, 2022, **51**, 4634–4643.

47 Ö. F. Erdem, M. Stein, S. Kaur-Ghumaan, E. J. Reijerse, S. Ott and W. Lubitz, *Chem.-A Euro. J.*, 2013, **19**, 14566–14572.

48 A. Silakov, M. T. Olsen, S. Sproules, E. J. Reijerse, T. B. Rauchfuss and W. Lubitz, *Inorg. Chem.*, 2012, **51**, 8617–8628.

49 A. Le Cloirec, S. P. Best, S. Borg, S. C. Davies, D. J. Evans, D. L. Hughes and C. J. Pickett, *Chem. Commun.*, 1999, **1**, 2285–2286.

50 E. J. Lyon, I. P. Georgakaki, J. H. Reibenspies and M. Y. Daresbourg, *Angew. Chem., Int. Ed.*, 1999, **38**, 3178–3180.

51 F. Gloaguen, J. D. Lawrence, M. Schmidt, S. R. Wilson and T. B. Rauchfuss, *J. Am. Chem. Soc.*, 2001, **123**, 12518–12527.

52 C. Esmieu and G. Berggren, *Dalton Trans.*, 2016, **45**, 19242–19248.

53 J. D. Lawrence, H. Li, T. B. Rauchfuss, M. Bénard and M.-M. Rohmer, *Angew. Chem., Int. Ed.*, 2001, **40**, 1768–1771.

54 B. C. Manor, M. R. Ringenberg and T. B. Rauchfuss, *Inorg. Chem.*, 2014, **53**, 7241–7247.

55 G. Berggren, A. Adamska, C. Lambertz, T. R. Simmons, J. Esselborn, M. Atta, S. Gambarelli, J.-M. Mouesca, E. Reijerse, W. Lubitz, T. Happe, V. Artero and M. Fontecave, *Nature*, 2013, **499**, 66–69.

56 J. Esselborn, C. Lambertz, A. Adamska-Venkatesh, T. Simmons, G. Berggren, J. Noth, J. Siebel, A. Hemschemeier, V. Artero, E. Reijerse, M. Fontecave, W. Lubitz and T. Happe, *Nat. Chem. Biol.*, 2013, **9**, 607–609.

57 R. Gilbert-Wilson, J. F. Siebel, A. Adamska-Venkatesh, C. C. Pham, E. Reijerse, H. Wang, S. P. Cramer, W. Lubitz



and T. B. Rauchfuss, *J. Am. Chem. Soc.*, 2015, **137**, 8998–9005.

58 J. F. Siebel, A. Adamska-Venkatesh, K. Weber, S. Rumpel, E. Reijerse and W. Lubitz, *Biochemistry*, 2015, **54**, 1474–1483.

59 J. Esselborn, N. Muraki, K. Klein, V. Engelbrecht, N. Metzler-Nolte, U.-P. Apfel, E. Hofmann, G. Kurisu and T. Happe, *Chem. Sci.*, 2016, **7**, 959–968.

60 A. Adamska-Venkatesh, S. Roy, J. F. Siebel, T. R. Simmons, M. Fontecave, V. Artero, E. Reijerse and W. Lubitz, *J. Am. Chem. Soc.*, 2015, **137**, 12744–12747.

61 C. Esmieu, M. Guo, H. J. Redman, M. Lundberg and G. Berggren, *Dalton Trans.*, 2019, **48**, 2280–2284.

62 A. S. Pandey, T. V. Harris, L. J. Giles, J. W. Peters and R. K. Szilagyi, *J. Am. Chem. Soc.*, 2008, **130**, 4533–4540.

63 J. C. Lansing, J. M. Camara, D. E. Gray and T. B. Rauchfuss, *Organometallics*, 2014, **33**, 5897–5906.

64 D. J. Crouthers, J. A. Denny, R. D. Bethel, D. G. Munoz and M. Y. Daresbourg, *Organometallics*, 2014, **33**, 4747–4755.

65 M. Wang, L. Chen and L. Sun, *Energy Environ. Sci.*, 2012, **5**, 6763–6778.

66 B. Kumar, M. Beyler, C. P. Kubiak and S. Ott, *Chem.—A Euro. J.*, 2012, **18**, 1295–1298.

67 R. Mejia-Rodriguez, D. Chong, J. H. Reibenspies, M. P. Soriaga and M. Y. Daresbourg, *J. Am. Chem. Soc.*, 2004, **126**, 12004–12014.

68 G. Si, W.-G. Wang, H.-Y. Wang, C.-H. Tung and L.-Z. Wu, *Inorg. Chem.*, 2008, **47**, 8101–8111.

69 C. Esmieu and G. Berggren, *Dalton Trans.*, 2016, **45**, 19242–19248.

70 S. Dey, A. Rana, S. G. Dey and A. Dey, *ACS Catal.*, 2013, **3**, 429–436.

71 F. Quentel, G. Passard and F. Gloaguen, *Energy Environ. Sci.*, 2012, **5**, 7757–7761.

72 C. Di Giovanni, W. A. Wang, S. Nowak, J. M. Grenèche, H. Lecoq, L. Mouton, M. Giraud and C. Tard, *ACS Catal.*, 2014, **4**, 681–687.

73 S. Ott, M. Kritikos, B. Åkermark, L. Sun and R. Lomoth, *Angew. Chem., Int. Ed.*, 2004, **43**, 1006–1009.

74 S. Dey, A. Rana, D. Crouthers, B. Mondal, P. K. Das, M. Y. Daresbourg and A. Dey, *J. Am. Chem. Soc.*, 2014, **136**, 8847–8850.

75 M. E. Ahmed, S. Dey, M. Y. Daresbourg and A. Dey, *J. Am. Chem. Soc.*, 2018, **140**, 12457–12468.

76 H. J. Redman, P. Huang, M. Haumann, M. H. Cheah and G. Berggren, *Dalton Trans.*, 2022, **51**, 4634–4643.

77 J. T. Kleinhaus, F. Wittkamp, S. Yadav, D. Siegmund and U.-P. Apfel, *Chem. Soc. Rev.*, 2021, **50**, 1668–1784.

78 T. B. Rauchfuss, *Acc. Chem. Res.*, 2015, **48**, 2107–2116.

79 C. A. Boyke, J. I. van der Vlugt, T. B. Rauchfuss, S. R. Wilson, G. Zampella and L. De Gioia, *J. Am. Chem. Soc.*, 2005, **127**, 11010–11018.

80 F. Gloaguen, J. D. Lawrence and T. B. Rauchfuss, *J. Am. Chem. Soc.*, 2001, **123**, 9476–9477.

81 A. Le Cloirec, S. C. Davies, D. J. Evans, D. L. Hughes, C. J. Pickett, S. P. Best and S. Borg, *Chem. Commun.*, 1999, 2285–2286.

82 F. Gloaguen, J. D. Lawrence, M. Schmidt, S. R. Wilson and T. B. Rauchfuss, *J. Am. Chem. Soc.*, 2001, **123**, 12518–12527.

83 L. C. Song, Z. Y. Yang, H. Z. Bian and Q. M. Hu, *Organometallics*, 2004, **23**, 3082–3084.

84 A. D. Becke, *Phys. Rev. A*, 1988, **38**, 3098–3100.

85 A. D. Becke, *J. Chem. Phys.*, 1993, **98**, 5648–5652.

86 J. P. Perdew, *Phys. Rev. B*, 1986, **33**, 8822–8824.

87 A. Adamska-Venkatesh, D. Krawietz, J. Siebel, K. Weber, T. Happe, E. Reijerse and W. Lubitz, *J. Am. Chem. Soc.*, 2014, **136**, 11339–11346.

88 S. J. Borg, J. W. Tye, M. B. Hall and S. P. Best, *Inorg. Chem.*, 2007, **46**, 384–394.

89 B. Sieklucka, R. Dziembaj and S. Witkowski, *Inorg. Chim. Acta*, 1991, **187**, 5–8.

90 B. Mondal, K. Sengupta, A. Rana, A. Mahammed, M. Botoshansky, S. Ghosh Dey, Z. Gross and A. Dey, *Inorg. Chem.*, 2013, **52**, 3381–3387.

91 A. Le Goff, V. Artero, B. Jousselme, P. D. Tran, N. Guillet, R. Métayé, A. Fihri, S. Palacin and M. Fontecave, *Science*, 2009, **326**, 1384–1387.

92 A. Lasia, *Int. J. Hydrogen Energy*, 2019, **44**, 19484–19518.

93 T. Shinagawa, A. T. Garcia-Esparza and K. Takanabe, *Sci. Rep.*, 2015, **5**, 1–21.

94 J. O. Bockris and E. C. Potter, *J. Electrochem. Soc.*, 1952, **99**, 169.

95 M. K. Harb, U.-P. Apfel, J. Kübel, H. Görls, G. A. N. Felton, T. Sakamoto, D. H. Evans, R. S. Glass, D. L. Lichtenberger, M. El-khateeb and W. Weigand, *Organometallics*, 2009, **28**(23), 6666–6675.

96 V. Fourmond, P.-A. Jacques, M. Fontecave and V. Artero, *Inorg. Chem.*, 2010, **49**, 10338–10347.

97 A. Aster, S. Wang, M. Mirmohades, C. Esmieu, G. Berggren, L. Hammarström and R. Lomoth, *Chem. Sci.*, 2019, **10**, 5582–5588.

98 J. A. Wright, L. Webster, A. Jablonskytè, P. M. Woi, S. K. Ibrahim and C. J. Pickett, *Faraday Discuss.*, 2011, **148**, 359–371.

99 M. E. Ahmed, A. Nayek, A. Križan, N. Coutard, A. Morozan, S. Ghosh Dey, R. Lomoth, L. Hammarström, V. Artero and A. Dey, *J. Am. Chem. Soc.*, 2022, **144**, 3614–3625.

100 J. A. Birrell, V. Pelmenschikov, N. Mishra, H. Wang, Y. Yoda, K. Tamasaku, T. B. Rauchfuss, S. P. Cramer, W. Lubitz and S. DeBeer, *J. Am. Chem. Soc.*, 2020, **142**, 222–232.

101 J. Rosenthal and D. G. Nocera, *Acc. Chem. Res.*, 2007, **40**, 543–553.

102 D. R. Weinberg, C. J. Gagliardi, J. F. Hull, C. F. Murphy, C. A. Kent, B. C. Westlake, A. Paul, D. H. Ess, D. G. McCafferty and T. J. Meyer, *Chem. Rev.*, 2012, **112**, 4016–4093.

103 B. E. Conway and B. V. Tilak, *Electrochim. Acta*, 2002, **47**, 3571–3594.

104 A. Dey, *J. Am. Chem. Soc.*, 2010, **132**, 13892–13901.

